Materials Science & Engineering A 766 (2019) 138330

Contents lists available at ScienceDirect

Materials Science & Engineering A

journal homepage: www.elsevier.com/locate/msea

Topology optimization and characterization of Ti6Al4V ELI cellular lattice structures by laser powder bed fusion for biomedical applications

A.M. Vilardell[a,*], A. Takezawa[b], A. du Plessis[c], N. Takata[d], P. Krakhmalev[a], M. Kobashi[d], I. Yadroitsava[e], I. Yadroitsev[e]

[a] Karlstad University, Department of Engineering and Physics, Karlstad SE-651 88, Sweden
[b] Department of Transportation and Environmental Systems, Graduate School of Engineering, Hiroshima University, 1-4-1 Kagamiyama, Higashi-Hiroshima, Hiroshima, 739-8527, Japan
[c] CT Scanner Facility and Physics Department, Stellenbosch University, Stellenbosch, 7602, South Africa
[d] Department of Materials Process Engineering, Graduate School of Engineering, Nagoya University, Furo-cho, Chikusa-ku, Nagoya, 464-8603, Japan
[e] Department of Mechanical and Mechatronics Engineering, Central University of Technology, Bloemfontein, 9301, South Africa

ARTICLE INFO

Keywords:
Topology optimization
Cellular lattice structures
Laser powder bed fusion
Ti6Al4V
Elastic modulus
Compression strength

ABSTRACT

Topology optimization approach was used for the design of Ti6Al4V ELI lattice structures with stiffness and density close to the human bone for implant applications. Three lattice designs with volume densities of 35 %, 40 % and 45 % and corresponding elastic modulus of 18.6 GPa, 23.1 GPa 27.4 GPa close to the human bone were generated. Laser powder bed fusion (LPBF) technique was used for the manufacturing of the specimens. Physical measurements and mechanical characterization of specimens were assessed by microCT analyses and compression test, perpendicular and parallel to the building direction of the specimens.

LPBF Ti6Al4V ELI manufactured lattice structures showed deviations in wall thickness in comparison with the generated designs, leading to an increase in relative porosity but also a decrease in elastic modulus in comparison with the original designs. Horizontal walls of the lattice structures showed higher wall thickness in comparison with the vertical walls, leading to anisotropic behaviour of the lattice structures. Higher elastic modulus and compression strength were obtained when thicker walls were oriented along the loading direction of the compression test, showing a complete failure by dividing the specimens into two neighbouring halves. All specimens showed 45° diagonal shear fracture along the structure. On the other hand, higher energy absorption at first maximum compression strength peak was observed when samples were tested parallel to the building direction (when thinner walls were oriented along the loading compression direction). Results showed that designed lattice structures can possess the levels of human bones' stiffness and therefore can reduce/avoid stress shielding on implant applications.

1. Introduction

Laser powder bed fusion (LPBD) is an additive manufacturing (AM) technique that offers freedom in part-design, thus leading to the manufacturing of complex geometries and lightweight structures, such as cellular lattice structures, which have generated a hotspot interest for industrial and medical applications [1,2]. Cellular lattice structures (CLS) have high performance by achieving high strength-to-weight ratio but also by reducing the building time and energy consumption during the LPBF process [3,4].

Titanium (Ti) and its alloys, especially Ti6Al4V, are commonly used for implant applications due to their excellent biocompatibility, corrosion resistance and mechanical properties. Ti6Al4V alloy has a low elastic modulus (~110 GPa) in comparison with other metallic alloys used for implants such as 316 stainless steel (~210 GPa) and Co–Cr–Mo alloys (~240 GPa), which is beneficial to reduce the stress shielding effect of implants. The difference in elastic modulus between the bone (cortical bone - 17 GPa; trabecular bone - 11 GPa [5]) and implants induces an unfavourable stress distribution at the bone-implant interface, leading to the reduction of bone density in the vicinity of the interface [6]. The use of CLS is a good alternative to reduce the effective elastic modulus of the implant, and as a consequence, to reduce the stress shielding effect. Additionally, the use of lattice structures at the interface of the implant and the bone is beneficial for osseointegration, thus promoting bone in-growth [7]. Another method being investigated to reduce the effective elastic modulus of the implant is to alloy Ti with

* Corresponding author.
E-mail address: Amvilardell.research@gmail.com (A.M. Vilardell).

https://doi.org/10.1016/j.msea.2019.138330
Received 17 June 2019; Received in revised form 22 August 2019; Accepted 24 August 2019
Available online 26 August 2019
0921-5093/

another elements. For example, tantalum (Ta) has been reported to stabilize the β-phase in TiTa alloy, as well as to decrease the elastic modulus (down to 75 GPa, in a bulk material) [8]. The long-term process of developing standards for new materials, and for approving these new materials for implantation, is associated with intensive studies of the cytotoxicity of the materials, their behaviour in such a corrosive environment as the human body, confidence in the mechanical properties and the corresponding phases and microstructures suggesting all requirements. LPBF gives an opportunity to use approved materials that can be used for implantation, creating porous structures with densities and elastic modulus close to the human bone which can be tailored by the patient.

Ti6Al4V lattice structures have been of great interest in the last few years. The design of implants with desired microstructural, mechanical and biological properties is currently under research [9–11]. Different data has been published on the influence of strut diameter, percentage of density/porosity and size of the unit cell [12], as well as the influence of post-heat treatment on the microstructure and mechanical properties [13,14]. Recently, different design strategy approaches for implants such as CAD-based and image-based designs or, implicit surface modelling and topology optimization have been developed to replicate the biomechanical properties of the host bone [15]. Topology optimization has emerged as one of the powerful and useful tool for the design of structures. It can modify an existing design by incorporating explicit features into it and generate a completely new one with the desired features [16]. Most of the examples of the use of topology optimization can be found within structural compliance and multiphasic problems. The design of lattice structures by topology optimization is beneficial in order to obtain optimized light-weight structures with the desired design, structure and structural properties for a specific application. Within biomedical field, the optimization procedure for designing lattice structures with desired pore size, porosity/density percentage [17], as well as a stiffness close to the host bone [18,19] is required for implant applications.

The goals of the present research are to: (i) topology optimize, (ii) print by LPBF technique and (iii) characterize the microstructure and mechanical properties of novel CLS designs for implant applications with density and stiffness close to the human bone. A total of three different CLS designs converged through topology optimization with density percentages of 35, 40 and 45 %, corresponding to effective elastic modulus of 18.6 GPa, 23.1 GPa and 27.4 GPa, respectively. The percentage of density, as well as elastic modulus values were chosen according to bone properties [20,21].

2. Materials and experimental methods

2.1. Topology optimization of cellular lattice structures

The applied criteria of topology optimization for the design of the lattice structure was a stiffness close to the human bone, as well as high porosity. For that purpose, it was stablished a stiffness value of E = 20 GPa and porosity higher than 50 %. The cell unit was assumed to be periodically repeated. The static elastic deformation of a metal with isotropic stiffness was first considered for the calculation of effective stiffness of lattice structure. The micro-scale linear elastic deformation of the lattice structure was assumed to follow Hooke's law:

$$\sigma_{ij} = C_{ijkl}\varepsilon_{kl} = C_{ijkl}\frac{\partial u_k}{\partial x_l} \tag{1}$$

where σ, C, ε and u are the stress tensor, elastic tensor, strain tensor, and displacement vector, respectively. By solving this equation numerically using finite element methods (FEM) with Dirichlet boundary conditions ($u = 0$), the distribution of displacements u in the internal structure was obtained.

Macroscopic properties of the periodic structure can be calculated with numerical homogenization [22]. The effective elastic tensor C^H of the periodic structure composed of a unit cell Y is:

$$C^H_{ijkl} = \frac{1}{Y}\int_Y \left(C_{ijkl} - C_{ijpq}\frac{\partial \chi^{kl}_p}{\partial y_q}\right)dY \tag{2}$$

where, χ is the displacements obtained by solving the problem of Y periodic cells:

$$\int_Y C_{ijpq}\left(\delta_{pk}\delta_{ql} - \frac{\partial \chi^{kl}_p}{\partial y_q}\right)\frac{\partial v_i}{\partial y_j}dY = 0 \tag{3}$$

Here, ν is an arbitrary test function. Equation (2) was derived from the macroscopic Hooke's law $\sigma^H_{ij} = C^H_{ijkl}\varepsilon^H_{kl}$ when macroscopic strain ε^H_{kl} was a unit strain. Equation (3) is the equilibrium equation with prescribed unit strain.

A phase-field-based topology optimization method [23] was used to optimize the shape of the lattice base cell structure which was successful in the design of isotropic stiffness close to the bone lattice structure [24]. In the phase-field method, the base cell shape was represented as a distribution of the density function. Optimization was performed by representing properties as a function of the density function φ. For example, the local micro-scale elastic modulus E of a unit cell composed of a metal with elastic modulus E_o and air (with zero stiffness) was expressed in terms of the density function φ; $(0 \le \varphi \le 1)$:

$$E = \varphi^p E_0 \tag{4}$$

where p is the penalization parameter (set to 3). The optimum shape of the pore structure is a distribution of φ, which is updated by solving the Allen-Cahn partial differential equation [25]:

$$\frac{\partial \varphi}{\partial t} = \kappa\nabla^2\varphi - P'(\varphi) \tag{5}$$

$$P(\varphi) = \frac{1}{4}Q(\varphi) + \eta R(\varphi),\ \ Q(\varphi) = \varphi^2(1-\varphi^2),\ R(\varphi) = \varphi^3(6\varphi^2 - 15\varphi + 10) \tag{6}$$

where t is the virtual time step of the design variable update, P is the asymmetric double-well potential with minima at 0 and 1, and η is a positive coefficient. Because of coupling between the diffusion and reaction terms in (5), φ was divided into several domains that correspond to 0 or 1. The phase-field interface that corresponds to the intermediate values $0 < \varphi < 1$ exists between these domains. The interface moves in the normal direction according to the shape of the double-well potential. That is, the interface evolves in the direction of lower minimum potential.

In the present manuscript, it was designed an isotropic lattice structure with a density and stiffness close to the human bone. The elastic tensor in an insotropic material was represented by two independent variables. Thus, to obtain effective isotropic stiffness, the penalty term, represented as the error between the current effective elastic tensor and the isotropic state [26], was added to the objective function as a penalty term. The optimization problem was then formulated with an added unit cell volume fraction constraint as follows:

$$\text{minimize } -\kappa^H + P_{iso} \tag{7}$$

where,

$$\kappa^{\mathrm{H}} = \sum_{i=1}^{3}\sum_{j=1}^{3} C^H_{ij} \tag{8}$$

$$P_{\mathrm{iso}} = \frac{1}{6}\sum_{i=1}^{3} C^H_{ii} - \frac{1}{12}\sum_{i=1}^{3}\sum_{j=1}^{3}(1-\delta_{ij})C^H_{ij} - \frac{1}{3}\sum_{i=4}^{6} C^H_{ii} \tag{9}$$

Subject to,

$$\frac{\int_\Omega \varphi dx}{\int_\Omega dx} \le V_{\max} \tag{10}$$

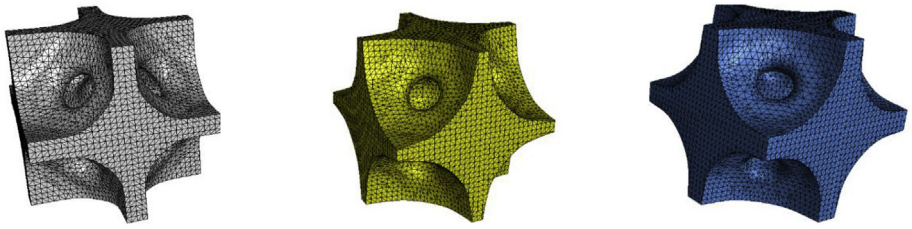

(a) (b) (c)

Fig. 1. Unit cell designs obtained by topology optimization with three different density values: (a) 35 % (CLS 0.35), (b) 40 % (CLS 0.40) and (c) 45 % (CLS 0.45) for Ti6Al4V ELI alloy with effective elastic modulus of 18.6 GPa, 23.1 GPa and 27.4 GPa, respectively.

$0 \leq \varphi \leq 1$

where κ^{H} and P_{iso} are the effective bulk modulus and the penalty term with respect to the isotropy, Ω is the volume of the target unit cell, and V_{max} is the maximum volume fraction. The density function was updated based on the sensitivities of the objective function and the constraint. The sensitivities of these functions in (4) were derived based on the Adjoint variable method [27]. The optimization procedure was as follows. The characteristic displacement distribution in the unit cell was calculated by solving (1) by FEM with respect to the six types of prescribed unit strain. Then, the effective elastic tensor, the objective function, and the constraint were calculated. Sensitivities for the objective function and the constraint were also calculated. Finally, the density functions were updated by solving (5) using the finite difference method. These procedures were repeated until the iteration limit or specified convergence criteria were reached.

Fig. 1 shows the optimized results of the unit cell designs, effective elastic modulus vs. volume fraction. Inner holes (ø = 571 μm) were considered within the optimization to remove the powder after the manufacturing process. Three unit cell designs with an effective elastic modulus close to 20 GPa were selected for present study (Fig. 1). The selected unit cell designs have three different density/porosity percentages: 35 % (65 % porosity), 40 % (60 % porosity) and 45 % (55 % porosity), corresponding to an effective elastic modulus of 18.6 GPa, 23.1 GPa and 27.4 GPa, respectively, considering Ti6Al4V ELI alloy with elastic modulus of 115 GPa and Poison's ratio of 0.31.

2.2. Powder

CLS were manufactured with Ti6Al4V ELI powder from TLS Technik GmbH & Co Spezialpulver KG. The chemical composition was 6.31 wt. % of Al, 4.09 wt.% of V, 0.12% of O and Ti was a balance. The powder had a spherical morphology typical of the gas atomization process, and a particle size diameter of d_{10} = 12.6 μm, d_{50} = 22.9 μm and d_{90} = 37 μm. Before manufacturing, the powder was dried at 80 °C for 2 h.

2.3. Laser powder bed fusion manufacturing

CLS specimens were produced by selective laser melting SLM EOSINT M280 system (EOS GmbH) with a 200 W laser and original parameters Ti64_Performance 1.1.0 (30 μm powder layer thickness). A back-and-forth (zigzag) scanning strategy by strips of 5 mm in width with a hatch distance of 100 μm was applied. All the process occurred in an argon atmosphere. The oxygen level in the chamber was controlled, and it was in the range of 0.07–0.12%. All specimens, 20 × 20 × 20 mm in size, were built without supports, directly on the stainless steel base plate. A stress-relief treatment was performed in vacuum furnace at 650 °C during 3 h before the specimens were cut off from the base plate by using wire electrical discharge machining. The specimens were named, CLS 0.35, CLS 0.40 and CLS 0.45 according to their designed density percentages of 35 %, 40 % and 45 %.

2.4. Physical and microstructural measurements

The surface topography of LPBF lattice structures was investigated by field-emission scanning electron microscope (FE-SEM, Jeol JSM-6610A) operated at a voltage of 20 kV. The cross-sections of the samples were prepared by standard metallographic procedure: samples were grinded up to 4000 SiC paper, polished with colloidal silica, and etched with Kroll's reagent. An optical microscope (OM- Nikon ECLIPSE LV150 N) was used to investigate the wall thickness of the SLM lattice structures. As the wall thickness was not uniform along the unit cell (Fig. 1), the wall thickness of the middle and finest part of the wall was measured as a wall thickness. For every optical microscope micrograph, 10 dimensional values of the wall thickness were measured and average value was calculated. The microstructure of the samples was analysed by FE-SEM, and phase analysis was performed by using an electron backscatter diffraction (EBSD) at step sizes of 0.2 and 0.3 μm. EBSD samples were prepared by cutting thin lamellas of 10 × 7 × 1 mm and ion-polished them by a JEOL cross-section polisher at 6 V.

2.5. Mechanical characterization

Uniaxial compression test of CLS were carried out with 50 Ton press machine (Tokyo Koki Seizosho, Japan) according to ISO 13314 [28]. Tests were performed by applying a constant strain rate of 1.5 mm/min. The strain was measured by the actual displacement of the crossheads of the testing machine. A total of three specimens were tested for each CLS design (CLS 0.35, CLS 0.40 and CLS 0.45), at two orientations, parallel (PAR) or perpendicular (PER) to the LPBF building direction (BD). The compression tests were recorded to analyse the deformation behaviour of the samples. Mechanical properties, such as elastic modulus and compressive strength, and energy absorption were calculated according to the ISO 13314 [28].

2.6. MicroCT analyses

X-ray microCT was used for detailed analysis of the produced samples. X-ray microCT was reviewed recently for its use in characterization of additively manufactured components [29]. The system used in this work was a General Electric Vtomex L240, with image analysis performed using Volume Graphics VGStudio Max 3.2, as described in more detail in Ref. [30]. In this case the voxel size was set to 25 μm, with 2100 step positions during a full rotation of the sample – the first image at each new position was discarded and the next two averaged at 250 m s per acquisition to create a high quality image free of sample movement. Voltage was set to 200 kV with current 100 μA and 0.5 mm copper beam filtration. For more details on optimization of scan parameters the reader is referred to Ref. [31]. The total material volume fraction, as well as wall thickness of the lattice structures were calculated in order to be compared with the measured ones by optical microscopy but also with the CAD-designed ones. Linear measurements were made at the thinnest part of the wall corresponding to Fig. 1, and the 3D wall thickness measurements where made with the wall

thickness (sphere) function. Wall microporosity was measured using the defect analysis module, with minimum 27 voxels (3 × 3 × 3) which translates to minimum pore sizes detected of 75 μm for the whole-lattice scans. Therefore, selected small sections were scanned to gain insight into smaller microporosity. These small sections of 2 × 2 × 2 mm were scanned allowing micropores to be detected with a minimum diameter about 15 μm.

Additionally, the use of the structural mechanics simulation module in VGStudio Max was used to make direct finite element modelling on microCT voxel data. It allowed the calculation of the effective elastic modulus of the structure, including the different wall thickness values and other imperfections (e.g. warping of some areas, etc.). The algorithm used was an immersed-boundary finite element code and a simulation cell size of 80 μm was used. The direct voxel-based simulation method is relatively new but has been applied successfully in a few recent studies [32–34].

3. Results

3.1. Physical measurements of cellular lattice structures

The porosity values of the manufactured LPBF specimens were 10–14% higher than the designed ones (Table 1). This increase in porosity of the produced samples was mainly due to the decrease of wall thickness in Z direction (building direction). Fig. 2 shows those variations in minimum wall thickness by using microCT in comparison with designed geometry. The thinnest wall thickness of the lattice structures was found in CLS 0.40, followed by CLS 0.35 and 0.45 designed models. The same tendency was also observed in the manufactured specimens, but walls oriented perpendicular to the building direction showed thicker profiles and their average thickness values varied significantly. Parallel to the building direction, walls had lower thickness than the designed walls (Table 2).

Fig. 3a-b and 3c-d illustrate the differences in the vertical and horizontal wall thicknesses observed by OM and SEM, respectively. Vertical walls were thinner and closer to the designed wall thickness. The deviations between designed and experimental wall thickness could be explained by the analysis of the strategies selected by EOS software for the printing of vertical and horizontal walls. Fig. 3e illustrates the strategy of laser scanning of the printing of the thinnest parts of the vertical walls. To have designed thickness, which was about an accuracy limit according to EOS specification, the laser scanned the wall without hatching but with scanning parameters chosen for contour/upskin/downskin scanning. At printing of horizontal walls another scanning strategy was used, Fig. 3f. Horizontal walls even in its thinnest part were printed with hatch scanning. Additionally, a factor of overhanging and layer thickness contributed in some shape distortion and thickness of the horizontal walls. Since laser power and scanning speed are different in contour/upskin/downskin and hatch scanning, a difference in selected strategy to print vertical or horizontal walls resulted in a deviation in observed experimental thicknesses of the walls. Therefore, the manufacturing of thin walls requires other special scanning strategy with calibration equipment and need to take into account offsets and geometry of skins and contourings for accurate production of thin walls.

The microporosity of the walls was analysed more in detail. For that purpose, specimens were cut into small volume cubes (2 × 2 × 2 mm approximately) to be scanned at high resolution by microCT. Fig. 4 shows the microCT scan of one of those cubes (Fig. 4a), as well as the distribution of its inner porosity and pore size diameter (Fig. 4b). The three lattice structure designs showed similar results, which was expected as same process parameters were used and designs were very similar. An average value of 0.12 ± 0.04 vol% microporosity was obtained. All pores were distributed evenly within the lattice structures. Most of the pores were below 45.3 μm, but a few coarse pores up to 244 μm in size were observed.

Table 1
Porosity values of the CLS designs (vol %).

Lattice designs	*Designed porosity*	*MicroCT measured porosity*
CLS 0.35	65.8	71.5 ± 0.006
CLS 0.40	61.0	67.6 ± 0.006
CLS 0.45	56.2	62.7 ± 0.003

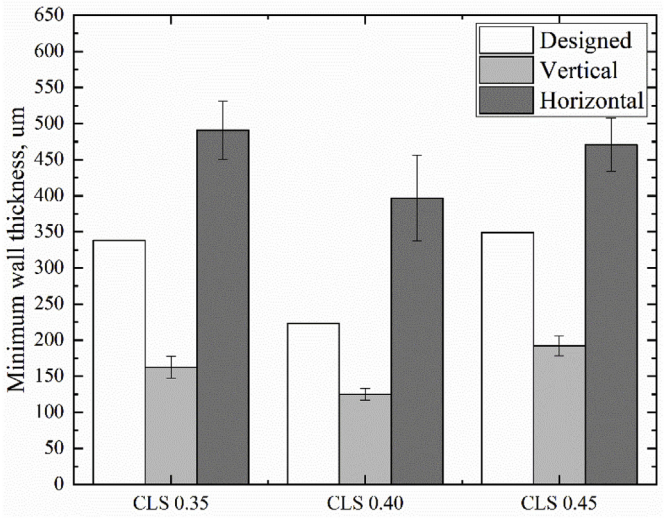

Fig. 2. Minimum wall thickness values of the CLS Ti6Al4V ELI designs in comparison with the vertical and horizontal wall thicknesses microCT measurements from LPBF manufactured specimens.

Table 2
Wall thickness values of the CLS designs.

Lattice designs	Designed wall thickness (μm)	MicroCT measurements of wall thickness (μm)	
		Vertical	*Horizontal*
CLS 0.35	338	162.3 ± 15	490.7 ± 40.3
CLS 0.40	223	124.9 ± 8	396.7 ± 59.4
CLS 0.45	349	192.1 ± 14	470.6 ± 36.9

3.2. Microstructural analyses of cellular lattice structures

Fig. 5 shows the EBSD phase maps of CLS 0.45 lattice structures specimens after stress-relief treatment. The high cooling rates of the LPBF manufacturing process led to the formation of metastable structures, in this case the typical needle-like shape α'-microstructure commonly observed in LPBF Ti6Al4V ELI. Additionally, it can be observed the growth of columnar prior β grains from the crystallization process from of β (from the liquid) to α'-phase, with a thickness value ~100 μm (Fig. 3a–b). Several columnar grains can be observed within each wall. EBSD analyses present a small amount of β-phase after stress-relief treatment (0.8–1.5%) and it appears localized at the grain boundaries of needle-shaped α' grains (Fig. 5). This can be explain by: (i) the heat up and cool down cycling of the LPBF manufacturing process which can result in the initiation of decomposition of the α'-phase [35], or (ii) decomposition of the α' phase during stress-relief treatment [36].

3.3. Mechanical assessment: compression tests

3.3.1. Deformation behaviour

Compression tests were recorded during all their performance to analyse the deformation and fracture behaviour of the specimens. Fig. 6

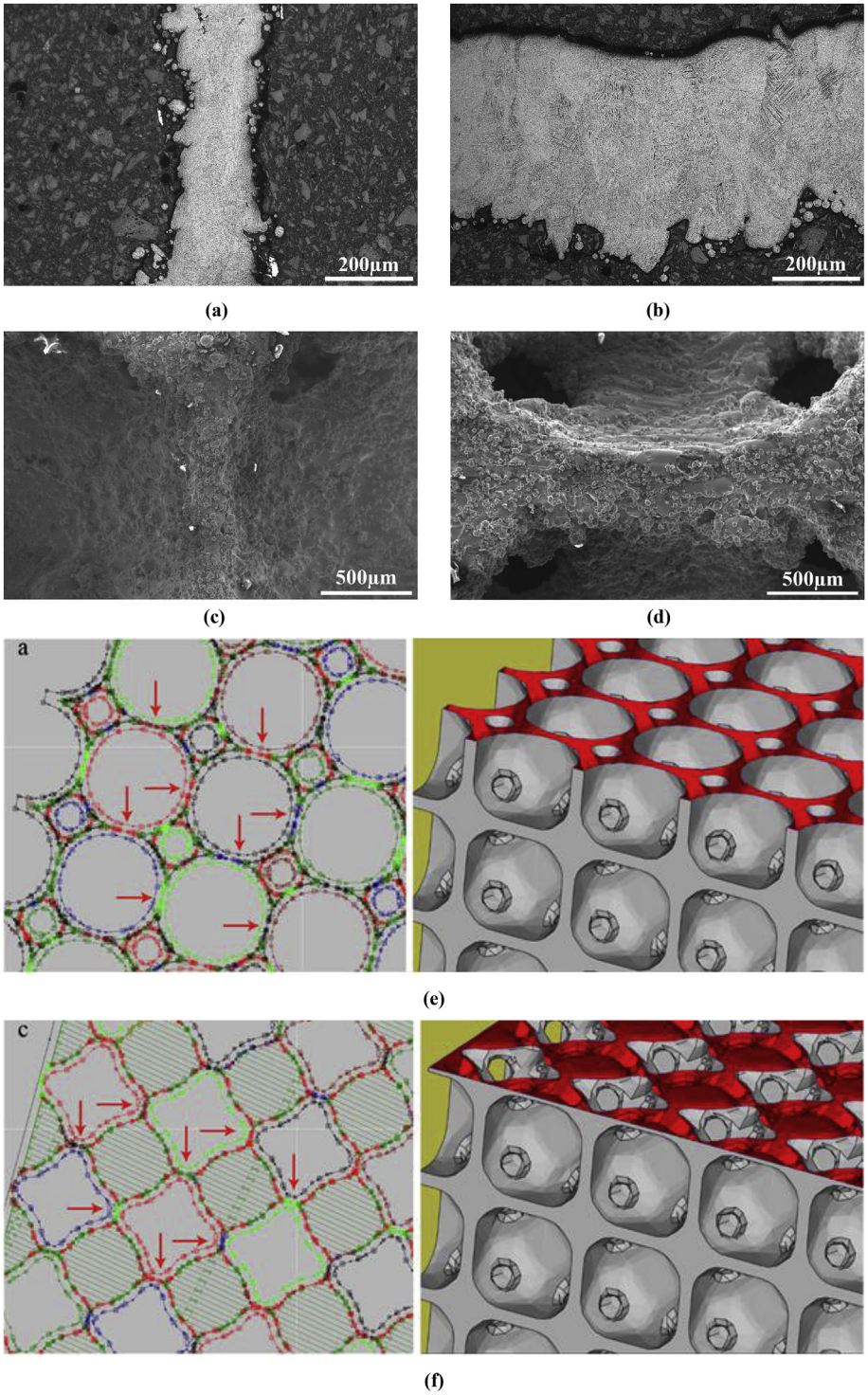

Fig. 3. (a–b) Optical and (c–d) SEM micrographs of vertical and horizontal walls of CLS 0.45 specimen. (e) Scanning strategy of EOSINT M280 scanning procedure of the minimum wall thickness region and for (f) the next layers where walls increased their thickness.

shows the images taken at different strain percentages during the compression test. Below 7 % strain, it can be generally observed that lattice structures deformed to a barrel shape under compression loading, attributed to the increased of lateral resistance provided by the lattice network against horizontal deformation (Fig. 6b). Specimens tested parallel to the BD, where thinner walls were oriented parallel to the loading direction, showed higher bending and stretching of the vertical and horizontal walls than specimens tested perpendicular to the BD. Detailed observations showed that vertical walls from the outer part of the lattice structure suffered higher bending deformation than the middle ones. On the other hand, it was observed that horizontal walls located in the middle of the structure suffered higher stretching than the ones places on the top and bottom sides.

Specimens started deform plastically around 2 % strain, in all specimens and conditions. Further compression led to higher plastic deformation, and the structure of the specimens ended collapsing around 8 % strain showing brittle diagonal shear failure (45°) across the entire structure (Fig. 6c). At that point, small differences were observed

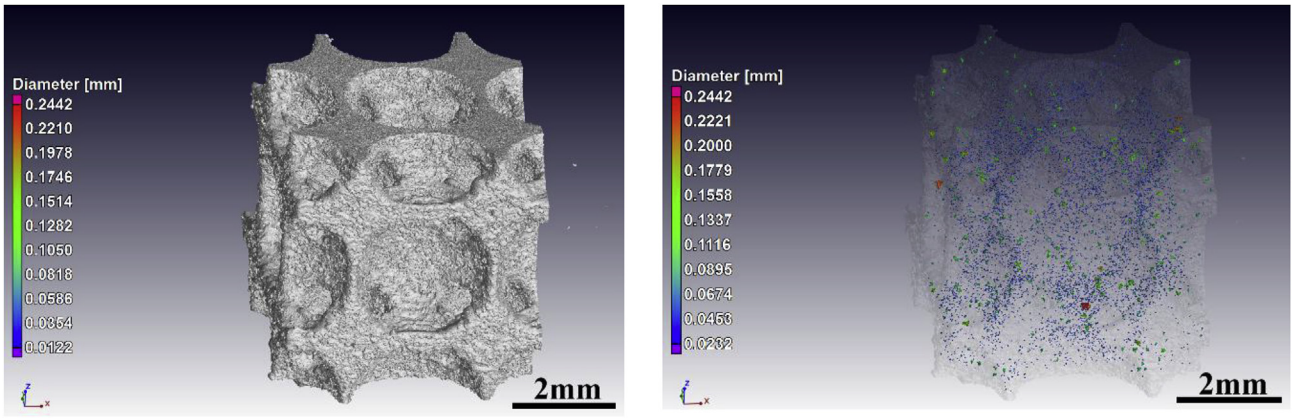

Fig. 4. MicroCT scan of 2 × 2 × 2 mm cube of 0.45 lattice design, showing the (a) surface view with surface roughness varying with orientation, and (b) internal microporosity evenly distributed across the structure, the largest pores of 244 μm in diameter are marked red. (For interpretation of the references to colour in this figure legend, the reader is referred to the Web version of this article.)

between samples tested parallel and perpendicular to the BD. Samples tested perpendicular to the BD exhibited a complete diagonal shear failure dividing the specimen in to two neighbouring halves zero load-bearing capability. Samples tested parallel to the BD, collapsed and started crushing at different points along the diagonal failure being able to retain load-bearing capability. At higher strains, lattice structures kept collapsing, and secondary fractures, mostly at 45° can be distinguished (Fig. 6d). Structures started densifying around 50 % strain (Fig. 6e). All three CLS designs behaved similarly under the compression tests by means of deformation behaviour.

Fig. 7 shows the stress-strain curves for the specimens tested perpendicular (PER) and parallel (PAR) to the BD. Stress-strain curves showed the existence of three distinct stages: (i) the elastic–plastic deformation, (ii) fluctuation and (iii) densification. CLS showed a first maximum compressive strength peak followed by a sharp drop to low-stresses between 5 and 8 % strain (corresponding to Fig. 6b and c, respectively). Results showed that compressive strength increased with the increase of volume density of the lattice structure, reaching higher compressive strength for CLS 0.45 specimens, followed by CLS 0.40 and CLS 0.35 in both tested orientations. However, specimens with the same volume density showed higher compressive strength when were tested perpendicular than parallel to the BD. This fact is attributed to the orientation of thinner and thicker walls during the compression test. Higher compressive strengths were obtained when thinner walls were placed perpendicular to the BD (PER-0.35, PER-0.40, PER-0.45), and lower compressive strength were obtained when thinner walls were placed parallel to the BD (PAR-0.35, PAR-0.40, PAR-0.45).

Following the first maximum compressive strength peaks, the structure of the specimens collapsed resulting in a low loading capacity of the samples after plastic failure. The load-bearing capacity was calculated for all speciments tested PAR and PER to BD by coefficient K, defined as $K = \frac{\sigma_{min}}{\sigma_b}$, where $\sigma_{\min}$ is the first lowest value of stress after the initial plastic failure and σ_b is the compression strength [37]. The maximum and minimum loading capabilities corresponded to 1 and 0, respectively.

Results showed a decrease of loading bearing capability with the increase of wall thickness (Fig. 8). Specimens tested parallel to the building direction, where thinner walls were oriented along loading direction, showed a load bearing capacity in the range of 0.2–0.5. CLS 0.40 showed higher values since the lattice structured had the thinnest walls, followed by CLS 0.35 and 0.45. Specimens tested perpendicular to the building direction showed zero load bearing capacity since the specimens broke in two halves during compression test, except for CLS 0.35 that showed low loading capacity probably due to the higher porosity (65 %) in comparison with CLS 0.40 and CLS 0.45.

At higher compression strains (10–40 %), lattice structures demonstrated several increases/decreases of stress caused by secondary failures of the walls, most of them at 45° to the loading direction (Fig. 6d). Densification of the CLS started with strains higher than 40–50 % resulting in an increase of stress.

Fig. 5. EBSD phase maps of LPBF Ti6Al4V ELI lattice structure specimens after stress-relief treatment.

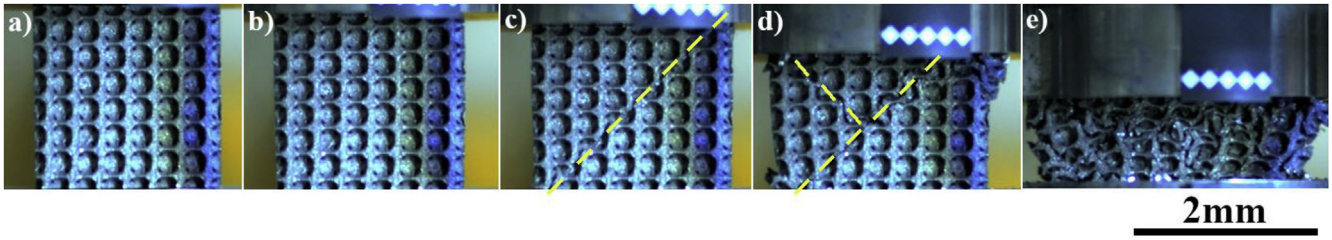

Fig. 6. Deformation behaviour of LPBF Ti6Al4V ELI lattice structure specimens at (a) 0 %, (b) 5 %, (c) 8 %, (d) 10–40 % and e) 50 % strains.

Table 3 shows the energy absorption of the lattice structures at first maximum compressive strength peak (prior to failure). The energy absorption capacity increased with the increase of the fraction volume density. At first maximum compressive strength peak, the energy absorption increased from 4 to 9.1 J/cm^3 and 3.2–8 J/cm^3 for specimens tested parallel and perpendicular to BD, respectively. Higher energy absorption values were obtained for specimens tested parallel to the BD since thinner walls were oriented parallel the loading direction leading to higher bending deformation in comparison with the thicker walls.

3.3.2. Elastic modulus and maximum stress of cellular lattice structures

Elastic modulus values were obtained through compression tests. Also, values were calculated by finite element modelling on microCT voxel data. Table 4 summarizes the elastic modulus values obtained from compression tests and microCT simulations, as well as compressive strength values obtained by compression test.

Elastic modulus values obtained by compression test and microCT simulations were lower than the designed ones. The differences in elastic modulus between designed and printed models can be explained by the obtaining of thinner walls that led to higher porosity within the lattice structures. Additional but rather insignificant effect could be due to microporosity in walls and surface topography. MicroCT results showed that LPBF samples tested perpendicular to the building direction had higher elastic modulus (19–38 %) than samples tested parallel to the building direction. Same trend was observed for the compression tests, showing an increase of elastic modulus between 22 and 35 % (Fig. 9). The increase of the elastic modulus with the increase of the volume density of the designed specimens was observed in microCT and compression tests results too. The highest elastic modulus was observed in the samples with the highest volume density (CLS 0.45), followed by CLS 0.40 and CLS 0.35. MicroCT results had standard deviations around ± 0.9 GPa, comparable with compression test results. The differences between elastic modulus results obtained by microCT simulations and compression test can be explained by the fine features not included in the microCT voxel simulation, such as surface notches or micro cracks, or lots of small pores smaller than voxel size. However, parameters such as microporosity, anisotropy and microstructure of the material could be contributed to those small differences too. The

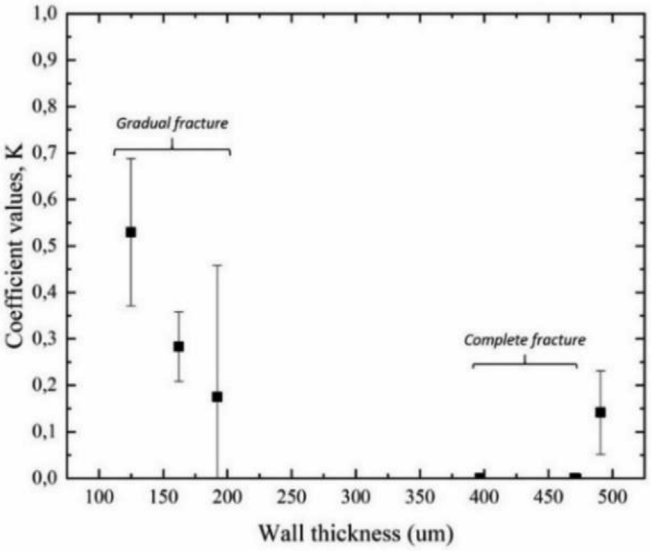

Fig. 8. Load-bearing capability (K) after the first plastic failure versus wall thickness of CLS.

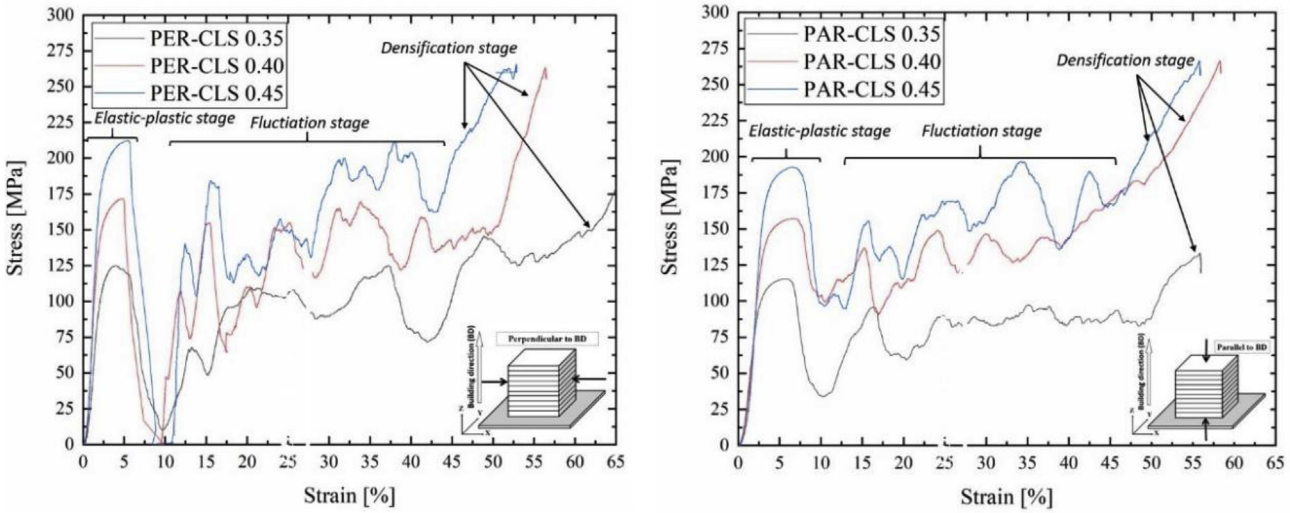

(a) **(b)**

Fig. 7. Compression strain-stress curves of LPBF Ti6Al4V ELI CLS specimens tested (a) perpendicular and (b) parallel to the BD.

Table 3
Energy absorption of LPBF Ti6Al4V ELI lattice structures.

ENERGY ABSORPTION [J/cm^3]		
Lattice designs	At first maximum compressive strength peak	
	PAR to the BD	*PER to the BD*
CLS 0.35	4 ± 0.5	3.2 ± 0.1
CLS 0.40	7.3 ± 0.4	6.2 ± 0.3
CLS 0.45	9.1 ± 0.8	8 ± 1

compressive strength of the lattice structures was observed to increase by 65–70% when the volume density increases from 35 % to 45 %, but increases 6–11 % within each volume density percentage when samples were tested perpendicular to BD (Table 4).

3.3.3. Failure mechanisms

Fig. 10a shows the microCT simulation of the stresses within the lattice structure during compression test. Stresses were mainly localized at the vertical walls but also in the inner part where powder remove holes were manufactured, creating a continuous line of stresses at 45° of the loading direction (Fig. 10a marked with dashed square). The highest stress areas from microCT simulations can be visualized in Fig. 10b with red colour in a side view. Most stress were located near the top, but some also in the corners near the bottom. The top view, Fig. 10b, shows most of the stress near the corners, which would explain the observed shear fracture occurring, starting at corners. This was observed previously for samples with different designs in a similar study using simulation, in that case the first failure location was identified at the corner of the sample, in samples which failed by shear [38].

Fig. 10c shows the 3D CAD model of 0.45 unit cell (Fig. 10c–i), but also its cross-section at two different points located at the ½ (ii) and 2/3 (iii) parts of the unit cell. Fig. 10c–iv plots the cross section of the entire lattice at 2/3 parts of unit cell. A termination of structural connectivity at 45° is observed within the lattice structure leading to a continuous area of stress, (Fig. 10c-dached red line), matching with the continuous stress area of Fig. 10a. Fig. 10d shows SEM micrograph of a fractured node. These observations may contribute also to the diagonal shear failure at 45°.

After all the analyses, different deviations were found between the designed and experimental results. Deviations in wall thickness of CLS, in both horizontal and vertical walls, led to an increase of porosity of the lattice structures. Thus, differences in elastic modulus were found between the designed and experimental values, but also between specimens tested parallel and perpendicular to the building direction. The discussion is focused on the understanding of the influence of those deviations on elastic modulus, as well as deformation behaviour and compressive strength on LPBF Ti6Al4V ELI lattice structures.

4. Discussion

The properties of lattices structures depend on material properties, their topology (connectivity) and the relative density of the structure

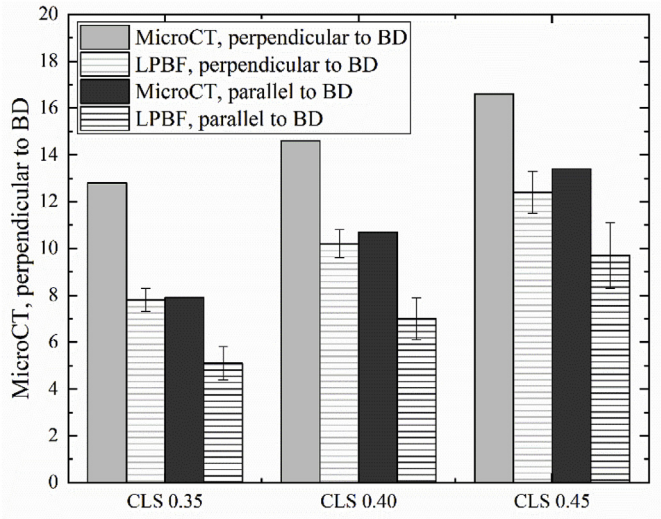

Fig. 9. Elastic modulus received with displacement of the crossheads of the testing machine in comparison with elastic modulus from microCT scans numerical simulations.

[39]. In the present study, three lattice structures were topology optimized to achieve a density and stiffness close to the human bone. The discussion takes into account those factors and is divided in the analyses of: (i) deformation behaviour and failure mechanism, (ii) elastic modulus and (iii) compression strength of LPBF Ti6Al4V ELI cellular lattice structures.

4.1. Deformation behaviour and failure mechanism

The topology of the cell structure influences load bearing capacity of the lattice structure and determines whether the applied load will result in predominantly bending or stretching of lattice structure. Stretch-dominant behaviour is known to provide higher strength and stiffness in comparison to bending-dominant behaviour, which has a better specific energy absorption [40]. “The ideals” of stretching- and bending-behaviours for lattices structures are stablished to correspond to an elastic modulus that scales relative density as $\rho/\rho s$ (slope 1) and $(\rho/\rho s)^2$ (slope 2), respectively [39]. However, in some occasions, some out of “the ideals” cases have been observed. FCCZ and FBCCZ lattice structures were classified to have bending-dominating behaviour according to Maxwell's stability, but experimental results showed that they have stretch-combined behaviour trends [41]. It has been noted that these formulae are only applicable to samples with relative density less than 30 % [42]. Although, the specimens of the present study have > 30 % relative density, it is possible to compare their deformation behaviours with other Ti6Al4V lattice structures in literature.

Failure behaviour of solid Ti6Al4V with diagonal crack was found to be due to the development of maximum shear stress oriented 45° diagonally to the direction of compression [43]. Similar brittle deformation behaviour has been observed in porous LPBF Ti6Al4V specimens during compressive deformation [41–46]. Choy et al. [42]

Table 4
Elastic modulus of CLS specimens.

Name	ELASTIC MODULUS [GPa]					MAX STRESS [MPa]	
	Designed EM	MicroCT		Compression test			
		PER to BD	*PAR to BD*	*PER to BD*	*PAR to BD*	*PER to BD*	*PAR to BD*
CLS 0.35	18.6	12.8	7.9	7.8 ± 0.5	5.1 ± 0.7	127 ± 2	114 ± 1.1
CLS 0.40	23.1	14.6	10.7	10.2 ± 0.6	7 ± 0.9	169.8 ± 2.1	159.3 ± 2.4
CLS 0.45	27.4	16.6	13.4	12.4 ± 0.9	9.7 ± 1.4	210.3 ± 3.4	194.4 ± 1.4

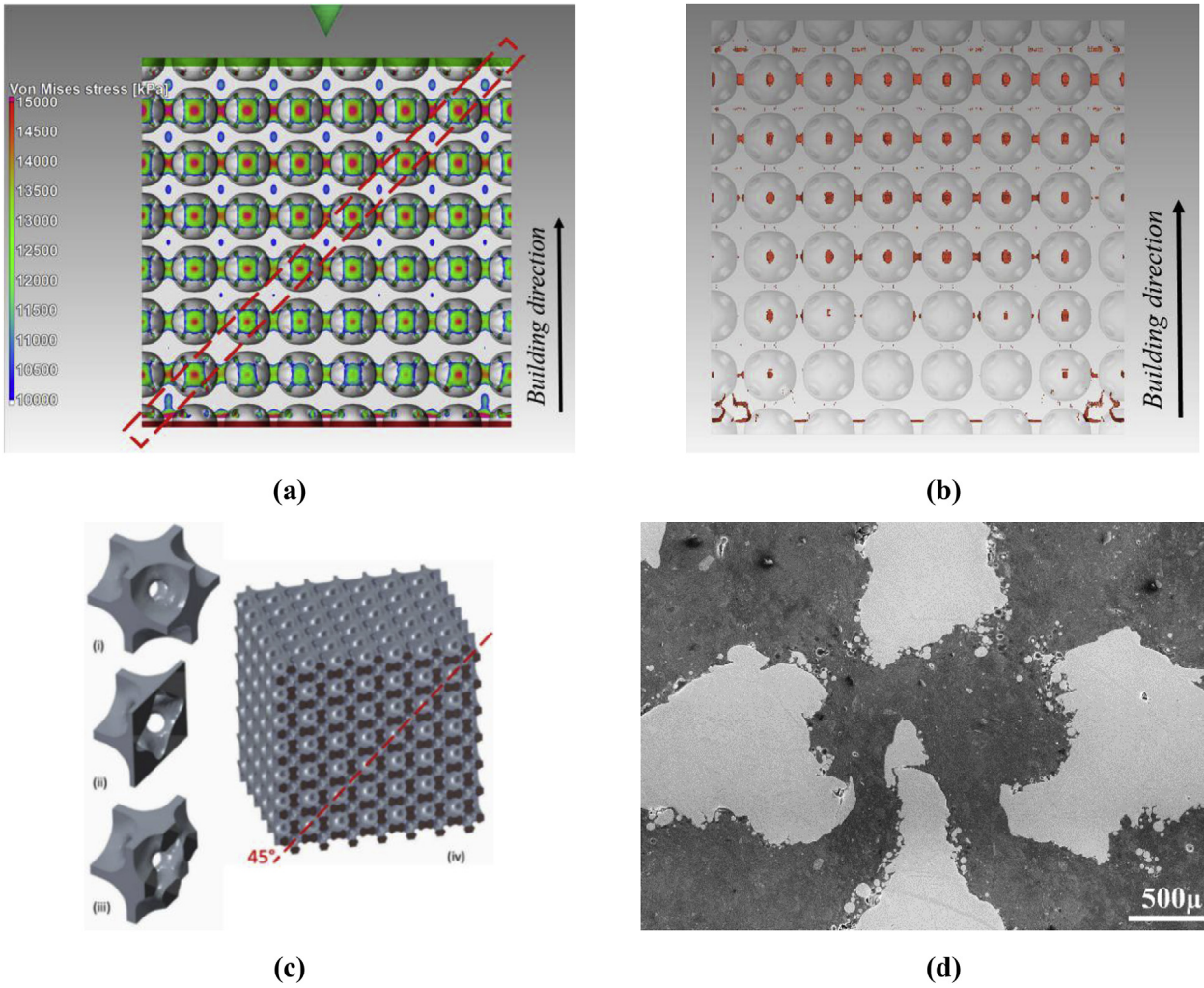

Fig. 10. MicroCT simulations of (a) the distribution of stresses, and (b) the highest stress areas showing most stress near top and near corners of CLS 0.45 specimen.; (c) cross sections of 3D CAD model of 0.45 cell unit and lattice structure; (d) SEM micrograph of the node fractured area after compression test.

reported that the deformation pattern of lattice structure is shifted from layer to layer to "V" shape shear band and towards diagonal crack as the density of the structure increases. Finally the lattice behaves, similar as a solid part. The lattice structures of the present study reached volume densities between 35 and 45 %, and behaved like stretch-dominating behaviour. Lattices showed a high compressive strengths peaks and low energy absorption along the strain-stress curve due to the collapsing and fracturing of the structure. The fact that specimens reached higher compressive strengths is also related to cell topology, since it has been observed that vertical struts along the load enhance stretch-dominated behaviour in the lattice structures [37]. Mazur et al. [41] studied the deformation of different cubic unit cell lattice structures: body centred, face centred, and face and body centred cubic unit cells achieving new structures by the supplementary addition of horizontal and vertical struts. Failure modes occurred through pronounced bending of diagonal struts and buckling of vertical struts followed by strut fracture and subsequent lattice cell collapse predominantly across diagonal shear bands at 45°. However, a stiffer lattice structure (FBCCXYZ) showed horizontal layer failure at the base of the specimen, where horizontal and vertical struts were able to resist diagonal shear failure in the structure, desirable for energy absorbing applications.

The lattice structures in the present study showed an energy absorption at first maximum compressive strength peak between 3.2 and 9 J/cm^3 (depending on their volume density and the orientation of the lattice structures during compression test). Those results are close to the energy absorption of the human bone at first maximum compressive strength peak. It is reported that mechanical properties of the bone decrease with the age. The energy absorption of a human femur has been reported to decrease from 3.85 to 2.23 J/cm^3 with the age (from 20 to 29 to 80–89 years old correspondingly) [47]. In comparison with the obtained results, CLS 0.40 and 0.45 specimens overcome those results with values slightly above of the human femur. On the other hand, CLS 0.35 values are reaching the limit, depending on the type and the function of the bone.

4.2. Influence of wall thickness, porosity and microstructure on elastic modulus

Several researches reported differences in thickness deviation of LPBF Ti6Al4V lattice specimens [41,42,48]. During LPBF process unmelted particles are captured by the melt pool at the edge of the walls, especially on overhanging surfaces. The adhesion of powder affects the dimensional accuracy of lattice structures leading to a decrease of the designed porosity. The powder adhesion has been observed to be more severe on horizontal struts than diagonal struts, and differences up to 30 % in thickness strut diameter have been found [41]. However, possible compensation for the diameter reduction could be achieved by an appropriate increase of the strut diameter in the designed model at the affected location. On the other hand, some studies reported good accuracy on the printing of the lattice in comparison with the CAD

design [20,38].

Elastic modulus is highly influenced by relative volume density/relative porosity of the lattice structures. The deviations of wall thicknesses led to a decrease of relative density and a decrease in the elastic modulus. The influence of volume density on the elastic modulus has been reported several times [41,45]. Strut-based lattice structures with different arrangement of horizontal/vertical struts has shown an increase of elastic modulus from 0.15 to 2.8 GPa with an increase of relative density from 4.1 to 39.7 % [41]. Zhang et al. [45] studied the influence of scan line spacing (distance between struts) on porous structures. An increase of scan line spacing from 200 to 700 μm led to an increase of porosity from 10 to 45 %, decreasing the elastic modulus from 85 to 16 GPa. In the present case, topology/connectivity of the three different lattice designs was close enough, and differences between mechanical properties are mostly related to volume density, as well as the deviation of the wall thicknesses. However, studies reported that different topologies with the same volume density significantly led to different elastic modulus [38]. The elastic modulus of trabecular human differs on bone type but also location within the body, it was found that one of the lowest is the human vertebra (5.7 ± 1.6 GPa), and one of the highest the human greater trochanter (21.3 ± 2.1 GPa) [21]. The suggested lattice structures in the present study showed closer values to the human bone, thus avoiding or reducing stress-shielding effect.

The increase of wall thicknesses due to the attachment of unmelted particles increased the surface roughness as well as microporosity within the walls. A microporosity value of 0.12 ± 0.04 % was obtained for the present CLS, however it can still be considered insignificant to affect elastic modulus, especially since most of the pores were below a pore size of 45.3 μm. Microporosity of Ti6Al4V rhombic and diagonal lattice structures was reported to be small too (0.00136 % and 0.00429 %, respectively) to affect mechanical properties of the specimens [38].

The microstructure of CLS Ti6Al4V after stress-relief treatment was mostly composed by columnar α′-phase grains, with a small amount of β-phase (0.8–1.5%) between needles, probably coming from the thermo-cycling of the LPBF manufacturing process and following stress-relief treatment. It is hard to evaluate the influence of the priorβ grain orientation on mechanical properties as the differences in thickness deviations between vertical and horizontal walls has major effect on mechanical properties. Also, it is speculative to consider the effects of microstructure when thickness of the struts is relatively small (less or around 0.4 mm) [42]. However, change of phase constitution within the microstructure has been reported to have significant influence on elastic modulus and compressive strength. Ti6Al4V specimens obtained by LPBF and EBM techniques led to different microstructures due to the different cooling rates. Ti6Al4V cubic design lattice structures obtained by LPBF shown α'-martensitic microstructure with higher strength values than α + β microstructure obtained EBM [42]. Other mechanical properties, for example hardness, have been reported to decrease with the transformation of α'-martensitic to α + β phases in lattice structures [20].

4.3. Compressive strength

The compressive strength was observed to increase with volumetric density but also the topology of the lattice structure. Choy et al. [42] reached maximum stress values between 14-35 MPa, 72–98 MPa and 116–244 MPa for LPBF Ti6Al4V specimens that had relative density between 13-14 %, 20–22 % and 34–43 %, respectively for a cubic and honeycomb strut cell design.

Lattice structures with similar compression strength to the cortical and trabecular bone have been reported in the literature [20,41]. FBCCXYZ strut-based lattice designs with a density of 39.7 % reached a compression strength values of 125 MPa. However, at lower density (24.3 %), a decrease in compression strength down to 89 MPa was observed [41]. On the other hand, Yan et al. [20] obtained Gyroid and Diamond TPMS lattices with 80–95 % porosity and a modulus of 0.12–1.25 GPa comparable to trabecular bone. Attempts were also performed with commercial pure titanium, and compressive strength values between 20 and 350 MPa corresponding to porosity levels between 70 and 15 % were obtained. Considering that the porosity of the cortical bone is around 5–10 % and trabecular bone 50–95 %, compressive strength values between that porosity percentage reach were below 50 MPa [12]. In the present study, compressive strength results matches with the one to the cortical bone between 130-200 MPa [49].

To sum up, topological optimization resulted in the combination of properties that we wanted to achieve by means of bone properties requirements. Previous studies showed its good approach on the design and development of lattice structures [24]. However, further research need to be performed on the manufacturing of thin walls by means of printing and scanning strategies, to match theoretical and experimental results.

5. Conclusions

This works presents the topology optimization design, LPBF manufacturing and physical, microstructural and mechanical characterization of Ti6Al4V ELI lattice structures with stiffness and density close to the human bone for implant applications. The main findings were the ones that follows:

- The manufacturing of thin walls requires other special scanning strategy with calibration equipment and need to take into account offsets and geometry of skins and contourings for accurate production of thin walls.
- Deviations in wall thicknesses between designed and LPBF manufactured specimens negatively influenced mechanical properties due to the increase of relative porosity.
- Anisotropy of LPBF structures is enhanced by the differences in thickness between vertical and horizontal walls. Higher elastic modulus and compression strength were obtained when thicker walls were oriented along the loading direction of the compression test. However, slightly higher energy absorption was obtained when thinner walls were oriented along the loading direction of the compression test.
- The combination of volume densities > 30 % and vertical walls of CLS enhanced brittle failure behaviour similar to solid Ti6Al4V ELI material, leading to a diagonal 45° shear failure across the structure. A complete failure of CLS leading to two neighbouring halves was observed on stiffer lattices where thicker walls were oriented along the loading direction of the compression test with no loading bearing capacity. When thinner walls where oriented to the loading direction, structures collapsed and started crushing at different points along the diagonal failure being able to retain load-bearing capability.
- The influence of the microstructure on mechanical properties was hard to evaluate since deviations of wall thickness were quite significant during compression test and walls were too thin.
- The CLS 0.35, 0.40 and 0.45 exhibit comparable porosity with the human bone and elastic modulus in the range of 5.1–12.4 GPa. Therefore, compressive strengths and energy absorption were found to be in the range of 114–210 GPa and 3.2–9.1 J/cm^3, respectively, showing comparable values with the cortical bone too. The designed lattice structures can tailored the levels of human bones and therefore reduce/avoid stress shielding effect on implant applications.

Data availability

The raw/processed data required to reproduce these findings cannot be shared at this time as the data also forms part of an ongoing study.

Acknowledgements

Authors thank the Swedish Agency for Economic and Regional Growth, Grant No20201144, ATLAB - additive manufacturing laboratory at Karlstad University, and Region Värmland for financial support. Also, authors would like to thank the Postdoctoral Fellowships for Research in Japan (summer program 2018) from Japan Society for the Promotion of Science (JSPS).

This work supported by the South African Research Chairs Initiative of the Department of Science and Technology; National Research Foundation of South Africa (Grant № 97994). Samples were built in CRPM at Central University of Technology, Free State and authors would like to thank Mr. Johan Els and Mr. Dean Kouprianoff.

References

[1] T.D. Ngo, A. Kashani, G. Imbalzano, K.T.Q. Nguyen, D. Hui, Additive manufacturing (3D printing): a review of materials, methods, applications and challenges, Compos. B Eng. 143 (2018) 172–196.
[2] N. Guo, M.C. Leu, Additive manufacturing: technology, applications and research needs, Appl. Mach. Mater. 8 (2013) 215–243.
[3] S.L. Sing, J. An, W.Y. Yeong, F.E. Wiria, Laser and electron-beam powder-bed additive manufacturing of metallic implants: a review on processes, materials and designs: laser and electron-beam additive manufacturing of metallic implants, J. Orthop. Res. 34 (2016) 369–385.
[4] A. du Plessis, C. Broeckhoven, I. Yadroitsava, I. Yadroitsev, C.H. Hands, R. Kunju, D. Bhate, Beautiful and functional: a review of biomimetic design in additive manufacturing, Addit. Manuf. 27 (2019) 408–427, https://doi.org/10.1016/j.addma.2019.03.033.
[5] S.C. Cowin (Ed.), Bone Mechanics Handbook, second ed., CRC Press, Boca Raton, FL, 2001.
[6] M. Geetha, A.K. Singh, R. Asokamani, A.K. Gogia, Ti based biomaterials, the ultimate choice for orthopaedic implants – a review, Prog. Mater. Sci. 54 (2009) 397–425, https://doi.org/10.1016/j.pmatsci.2008.06.004.
[7] S. Van Bael, Y.C. Chai, S. Truscello, M. Moesen, G. Kerckhofs, H. Van Oosterwyck, J.-P. Kruth, J. Schrooten, The effect of pore geometry on the in vitro biological behavior of human periosteum-derived cells seeded on selective laser-melted Ti6Al4V bone scaffolds, Acta Biomater. 8 (2012) 2824–2834.
[8] S.L. Sing, W.Y. Yeong, F.E. Wiria, Selective laser melting of titanium alloy with 50 wt% tantalum: microstructure and mechanical properties, J. Alloy. Comp. 660 (2016) 461–470.
[9] K. Kadirgama, W.S.W. Harun, F. Tarlochan, M. Samykano, D. Ramasamy, M.Z. Azir, H. Mehboob, Statistical and optimize of lattice structures with selective laser melting (SLM) of Ti6AL4V material, Int. J. Adv. Manuf. Technol. 97 (2018) 495–510, https://doi.org/10.1007/s00170-018-1913-1.
[10] S.Y. Choy, C.-N. Sun, K.F. Leong, J. Wei, Compressive properties of functionally graded lattice structures manufactured by selective laser melting, Mater. Des. 131 (2017) 112–120.
[11] S. Merkt, C. Hinke, J. Bültmann, M. Brandt, Y.M. Xie, Mechanical response of TiAl6V4 lattice structures manufactured by selective laser melting in quasistatic and dynamic compression tests, J. Laser Appl. 27 (2015) S17006, https://doi.org/10.2351/1.4898835.
[12] L. Mullen, R.C. Stamp, W.K. Brooks, E. Jones, C.J. Sutcliffe, Selective Laser Melting: a regular unit cell approach for the manufacture of porous, titanium, bone in-growth constructs, suitable for orthopedic applications, J. Biomed. Mater. Res. B: Appl. Biomater. 89B (2009) 325–334.
[13] S.L. Sing, W.Y. Yeong, F.E. Wiria, B.Y. Tay, Characterization of titanium lattice structures fabricated by selective laser melting using an adapted compressive test method, Exp. Mech. 56 (2016) 735–748.
[14] R. Wauthle, B. Vrancken, B. Beynaerts, K. Jorissen, J. Schrooten, J.-P. Kruth, J. Van Humbeeck, Effects of build orientation and heat treatment on the microstructure and mechanical properties of selective laser melted Ti6Al4V lattice structures, Addit. Manuf. 5 (2015) 77–84, https://doi.org/10.1016/j.addma.2014.12.008.
[15] X. Wang, S. Xu, S. Zhou, W. Xu, M. Leary, P. Choong, M. Qian, M. Brandt, Y.M. Xie, Topological design and additive manufacturing of porous metals for bone scaffolds and orthopaedic implants: a review, Biomater 83 (2016) 127–141, https://doi.org/10.1016/j.biomaterials.2016.01.012.
[16] O.M. Querin, M. Victoria, C. Alonso, R. Ansola, P. Martí, Topology optimization as a digital design tool, Topology Design Methods for Structural Optimization, Elsevier, 2017, pp. 93–111, , https://doi.org/10.1016/B978-0-08-100916-1.00006-4.
[17] A. Radman, X. Huang, Y.M. Xie, Topology optimization of functionally graded cellular materials, J. Mater. Sci. 48 (2013) 1503–1510, https://doi.org/10.1007/s10853-012-6905-1.
[18] X.Y. Yang, X. Huang, J.H. Rong, Y.M. Xie, Design of 3D orthotropic materials with prescribed ratios for effective Young's moduli, Comput. Mater. Sci. 67 (2013) 229–237, https://doi.org/10.1016/j.commatsci.2012.08.043.
[19] X. Huang, A. Radman, Y.M. Xie, Topological design of microstructures of cellular materials for maximum bulk or shear modulus, Comput. Mater. Sci. 50 (2011) 1861–1870, https://doi.org/10.1016/j.commatsci.2011.01.030.
[20] C. Yan, L. Hao, A. Hussein, P. Young, Ti–6Al–4V triply periodic minimal surface structures for bone implants fabricated via selective laser melting, J. Mech. Behav. Biomed. 51 (2015) 61–73, https://doi.org/10.1016/j.jmbbm.2015.06.024.
[21] R. Oftadeh, M. Perez-Viloria, J.C. Villa-Camacho, A. Vaziri, A. Nazarian, Biomechanics and mechanobiology of trabecular bone: a review, J. Biomech. Eng. 137 (2015) 010802, , https://doi.org/10.1115/1.4029176.
[22] J.M. Guedes, N. Kikuchi, Preprocessing and postprocessing for materials based on the homogenization method with adaptive finite element methods, Comput. Methods Appl. Mech. Eng. 83 (2) (1990) 143–198.
[23] A. Takezawa, S. Nishiwaki, M. Kitamura, Shape and topology optimization based on the phase field method and sensitivity analysis, J. Comput. Phys. 229 (7) (2010) 2697–2718.
[24] A. Takezawa, Y. Koizumi, M. Kobashi, High-stiffness and strength porous maraging steel via topology optimization and selective laser melting, Addit. Manuf. 18 (2017) 194–202.
[25] S.M. Allen, J.W. Cahn, A microscopic theory for antiphase boundary motion and its application to antiphase domain coarsening, Acta Metall. 27 (1979) 1085–1095.
[26] V.J. Challis, A.P. Roberts, A.H. Wilkins, Design of three dimensional isotropic microstructures for maximized stiffness and conductivity, Int. J. Solids Struct. 45 (14) (2008) 4130–4146.
[27] E.J. Haug, K.K. Choi, V. Komkov, Design Sensitivity Analysis of Structural Systems, Academic Press, Orlando, 1986.
[28] ISSO 13314 - Mechanical Testing of Metals. Ductility Testing. Compression Test for Porous and Cellular Metals.
[29] A. du Plessis, C. Broeckhoven, Looking deep into nature: a review of micro-computed tomography in biomimicry, Acta Biomater. 85 (2019) 27–40.
[30] A. du Plessis, S.G. le Roux, A. Guelpa, The CT Scanner Facility at Stellenbosch University: an open access X-ray computed tomography laboratory, Nucl. Instrum. Methods Phys. Res. Sect. B Beam Interact. Mater. Atoms 384 (2016) 42–49, https://doi.org/10.1016/j.nimb.2016.08.005.
[31] A. du Plessis, C. Broeckhoven, A. Guelpa, S.G. le Roux, Laboratory x-ray micro-computed tomography: a user guideline for biological samples, GigaScience (2017), https://doi.org/10.1093/gigascience/gix027.
[32] A. Du Plessis, C. Broeckhoven, S.G. Le Roux, Snake fangs: 3D morphological and mechanical analysis by microCT, simulation, and physical compression testing, GigaScience 7 (2018) 1–8, https://doi.org/10.1093/gigascience/gix126.
[33] A. du Plessis, I. Yadroitsava, S.G. le Roux, I. Yadroitsev, J. Fieres, C. Reinhart, P. Rossouw, Prediction of mechanical performance of Ti6Al4V cast alloy based on microCT-based load simulation, J. Alloy. Comp. 724 (2017), https://doi.org/10.1016/j.jallcom.2017.06.320.
[34] J. Fieres, P. Schumann, C. Reinhart, Predicting failure in additively manufactured parts using X-ray computed tomography and simulation, Procedia Eng. 213 (2018) 69–78, https://doi.org/10.1016/J.PROENG.2018.02.008.
[35] W. Xu, M. Brandt, S. Sun, J. Elambasseril, Q. Liu, K. Latham, K. Xia, M. Qian, Additive manufacturing of strong and ductile Ti–6Al–4V by selective laser melting via in situ martensite decomposition, Acta Mater. 85 (2015) 74–84, https://doi.org/10.1016/j.actamat.2014.11.028.
[36] E. Sallica-Leva, R. Caram, A.L. Jardini, J.B. Fogagnolo, Ductility improvement due to martensite α′ decomposition in porous Ti–6Al–4V parts produced by selective laser melting for orthopedic implants, J. Mech. Behav. Biomed. Mater. 54 (2016) 149–158, https://doi.org/10.1016/j.jmbbm.2015.09.020.
[37] M. Zhao, F. Liu, G. Fu, D. Zhang, T. Zhang, H. Zhou, Improved mechanical properties and energy absorption of BCC lattice structures with triply periodic minimal surfaces fabricated by SLM, Materials 11 (2018) 2411, https://doi.org/10.3390/ma11122411.
[38] A. du Plessis, I. Yadroitsava, I. Yadroitsev, Ti6Al4V lightweight lattice structures manufactured by laser powder bed fusion for load-bearing applications, Opt. Laser. Technol. 108 (2018) 521–528, https://doi.org/10.1016/j.optlastec.2018.07.050.
[39] file:///C:/Users/annavila/Downloads/SUARD_2015_archivage.pdf.
[40] S. Zhu, L. Ma, B. Wang, J. Hu, Z. Zhou, Lattice materials composed by curved struts exhibit adjustable macroscopic stress-strain curves, Mater. Today Commun. 14 (2018) 273–281, https://doi.org/10.1016/j.mtcomm.2018.01.017.
[41] M. Mazur, M. Leary, S. Sun, M. Vcelka, D. Shidid, M. Brandt, Deformation and failure behaviour of Ti-6Al-4V lattice structures manufactured by selective laser melting (SLM), Int. J. Adv. Manuf. Technol. (2015), https://doi.org/10.1007/s00170-015-7655-4.
[42] S.Y. Choy, C.-N. Sun, K.F. Leong, J. Wei, Compressive properties of Ti-6Al-4V lattice structures fabricated by selective laser melting: design, orientation and density, Addit. Manuf. 16 (2017) 213–224, https://doi.org/10.1016/j.addma.2017.06.012.
[43] J.T. Hammer, Plastic Deformation and Ductile Fracture of Ti-6Al-4V under Variolus Loading Conditions, The Ohio State University, Degree Master of Science Academic, Department, 2012.
[44] X.Y. Cheng, S.J. Li, L.E. Murr, Z.B. Zhang, Y.L. Hao, R. Yang, F. Medina, R.B. Wicker, Compression deformation behavior of Ti–6Al–4V alloy with cellular structures fabricated by electron beam melting, J. Mech. Behav. Biomed. 16 (2012) 153–162, https://doi.org/10.1016/j.jmbbm.2012.10.005.
[45] S. Zhang, Q. Wei, L. Cheng, S. Li, Y. Shi, Effects of scan line spacing on pore characteristics and mechanical properties of porous Ti6Al4V implants fabricated by selective laser melting, Mater. Des. 63 (2014) 185–193, https://doi.org/10.1016/j.matdes.2014.05.021.
[46] S. Merkt, C. Hinke, J. Bültmann, M. Brandt, Y.M. Xie, Mechanical response of TiAl6V4 lattice structures manufactured by selective laser melting in quasistatic and dynamic compression tests, J. Laser Appl. 27 (2015) S17006, https://doi.org/10.2351/1.4898835.
[47] D.B. Burr, C.H. Turner, Biomechanical measurements in age-related bone loss, The Aging Skeleton, Elsevier, 1999, pp. 301–311, , https://doi.org/10.1016/B978-012098655-2/50028-4.
[48] C.-Y. Lin, T. Wirtz, F. LaMarca, S.J. Hollister, Structural and mechanical evaluations of a topology optimized titanium interbody fusion cage fabricated by selective laser melting process, J. Biomed. Mater. Res. A. 83A (2007) 272–279, https://doi.org/10.1002/jbm.a.31231.
[49] L.-C. Gerhardt, A.R. Boccaccini, Bioactive glass and glass-ceramic scaffolds for bone tissue engineering, Materials 3 (2010) 3867–3910, https://doi.org/10.3390/ma3073867.